Rotational energy transfer kinetics of optically centrifuged CO molecules investigated through transient IR spectroscopy and master equation simulations

Matthew R. Laskowski, Tara J. Michael, Hannah M. Ogden, Millard H. Alexander, and Amy S. Mullin*

Department of Chemistry and Biochemistry, University of Maryland, College Park, MD, USA 20742

*Corresponding author: mullin@umd.edu

Abstract

A combined experimental and theoretical study of quantum state-resolved rotational energy transfer kinetics of optically centrifuged CO molecules is presented. In the experiments, inverted rotational distributions of CO in rotational states up to J=80 were prepared using two different optical centrifuge traps, one with the full spectral bandwidth of the optical centrifuge pulses, and one with reduced bandwidth. The relaxation kinetics of the high-J tail of the inverted distribution from each optical trap was determined based on high-resolution transient IR absorption measurements. In parallel studies, master equation simulations were performed using state-to-state rate constants for CO-CO collisions in states up to J=90, based on data from double-resonance experiments for CO with J=0-29 and a fit to a statistical power exponential gap model. The model is in qualitative agreement with the observed relaxation profiles, but the observed decay rate constants are smaller than the simulated values by as much as a factor of 10. The observed decay rate constants also have a stronger J-dependence than predicted by the model. The results are discussed in terms of angular momentum and energy conservation, and compared to the observed orientational anisotropy decay kinetics of optically centrifuged CO molecules. Models for rotational energy transfer could be improved by including angular momentum effects.

I. Introduction

One hundred years ago, major strides were made toward understanding the physics of chemical reactions. At the 1922 Faraday Discussion on "The Radiation Theory of Chemical Action," Lindemann identified molecular collisions as the means by which reactive molecules are

activated, and deactivated.[1] The Lindemann mechanism is an important component of many chemical and physical phenomena. At same meeting, Langmuir urged chemists to take up the challenge of understanding the quantum nature of chemical reactions. The combination of collisional energy transfer and quantized molecular energy is at the heart of our modern understanding of reaction rates, and of current research activities to expand on that knowledge. Hinshelwood included the role of vibrational energy in reaction rates.[2] Rice, Ramsperger, Kassel, and, later, Marcus generalized Eyring's activated complex theory (now known as transition state theory) to include the partitioning of quantized molecular energy.[3-7] Our understanding of collisional energy transfer has advanced in the past 100 years. Initially, without experiments to measure energy transfer processes, the strong collision assumption was invoked, leading to overestimates of activation and deactivation rates. Today, modern experimental and theoretical tools enable state-resolved investigations of collisional energy transfer, leading to in-depth mechanistic information such as product state distributions and energy partitioning.

Research on the collisional relaxation of rotational energy has a long history, and is motivated by efforts to understand the physical and chemical nature of high energy, non-equilibrium environments such as flames, plasmas, and gas-phase lasers, and of the products of exothermic reactions.[8-29] At 300 K, most molecules have energy gaps ΔE between rotational states that are significantly smaller than the thermal energy and rotational energy transfer rates are large compared to rates for vibrational relaxation. Double-resonance and other techniques have been used to determine state-to-state rate constants for a number of systems and reveal common features about rotational energy transfer processes.[11-23] The rate constants are largest when the change in angular momentum ΔJ is small, and decrease with increasing ΔJ. When the collision energy is reduced, the state-to-state rate constants have narrower distributions in ΔJ.[19-23] At 300 K, rotational energy transfer of thermally populated states can occur on nearly every gas-kinetic collision because of small energy gaps between rotational states. In some cases, rotational energy transfer is faster than the gas-kinetic collision rate because of long-range attractive forces.[17-19] Several models based on energy gaps have been proposed to describe rotational energy transfer rate constants. These include the modified

exponential gap, statistical polynomial exponential gap, and energy corrected sudden with exponential-power gap models.[12, 24-29]

The optical centrifuge is an ultrafast laser-based technique that prepares gas-phase molecules in extreme rotational states that not accessible by other means at 300 K.[30] In this method, an intense optical field with linear polarization aligns molecules with the optical field and angularly accelerates them into extreme rotational states. Inverted rotational distributions of molecules are prepared, with rotational energies that may be well beyond what have been studied before. The rotational energy gaps for the centrifuged molecules are larger than the thermal energy, thereby opening a door for studying rotational energy transfer in a new regime. In this paper, we investigate the relaxation kinetics of optically centrifuged CO molecules initially prepared with rotational energies up to E_{rot}=12,000 cm^{-1} and with rotational quantum numbers up to J=80 through combined experimental and theoretical approaches. In experiments, the rotationally excited CO molecules were detected with high-resolution transient IR absorption spectroscopy. In simulations, we performed master equation calculations for CO-CO collisional relaxation to model the state-resolved collisional energy transfer and compare with the experimental results.

In 2021, we reported the nearly-nascent rotational distributions of CO molecules that were prepared in two different optical centrifuge traps.[31] One optical trap, denoted S1, used the full spectral bandwidth of centrifuge laser, and had appreciable intensity beyond an angular frequency of 6×10^{13} radians s^{-1}, as shown in the left-hand panel of Figure 1. The other optical trap, denoted S2, used a reduced spectral bandwidth, as shown in the right-hand panel of Figure 1, and its intensity dropped significantly at angular frequencies near 5×10^{13} radians s^{-1}. Because the angularly accelerating optical field is the excitation source, the optically centrifuged molecules rotate unidirectionally in the plane perpendicular to the laser propagation. The nearly-nascent distributions of optically centrifuged CO molecules are shown for the in-plane (IP) and out-of-plane (OOP) components, based on polarization-resolved, transient IR absorption measurements. The highest J-states in both distributions have profiles that track the intensity profile of the optical trap. The S1 trap produces CO in $J \leq$80, while the S2 trap has $J \leq$67. Here, we analyze the time-dependence of the IP distributions to determine state-resolved relaxation

kinetics for the optically centrifuged molecules. The S1 distribution reported previously was comprised of three separate distribution measurements.[31] For the kinetic analysis presented here, we use a single distribution measurement to avoid any ambiguities based on scaling the distributions to a reference state.

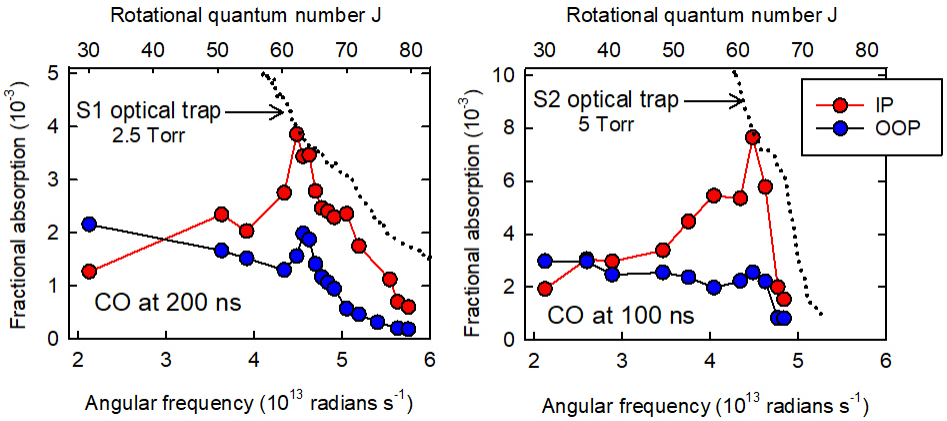

Figure 1. Transient IR absorption intensities for nearly-nascent CO rotational distributions prepared in two different optical centrifuge traps. The S1 trap (dotted line) uses the full spectral bandwidth of the pulse laser and populates CO states up to J=80. The S2 trap has reduced spectral bandwidth and populates CO states up to J=67. Both in-plane (IP) and out-of-plane (OOP) distributions are shown, relative to the plane of angular acceleration from the optical field. The populations have undergone approximately 5 gas kinetic collisions at the times shown.

II. Methods

Here, the experimental methods used for preparing CO in extreme rotational states and measuring the collisional relaxation kinetics of optically centrifuged molecules are described. The modeling methods used for the master equation simulations are also presented.

a. Experimental approach

Our optical-centrifuge transient-absorption spectrometer has been discussed in detail previously, and the key features of the instrument are presented here.[31,32] An ultrafast, amplified Ti:sapphire laser system provides pulses that are shaped into optical centrifuge pulses by controlling the chirp and polarization of the light. A high-resolution transient IR absorption spectrometer uses a quantum cascade laser for IR probing and active feedback control for

wavelength modulation. The optically centrifuged molecules are interrogated in a multipass (×11) IR detection region. Figure 2 shows the schematic of the instrumentation.

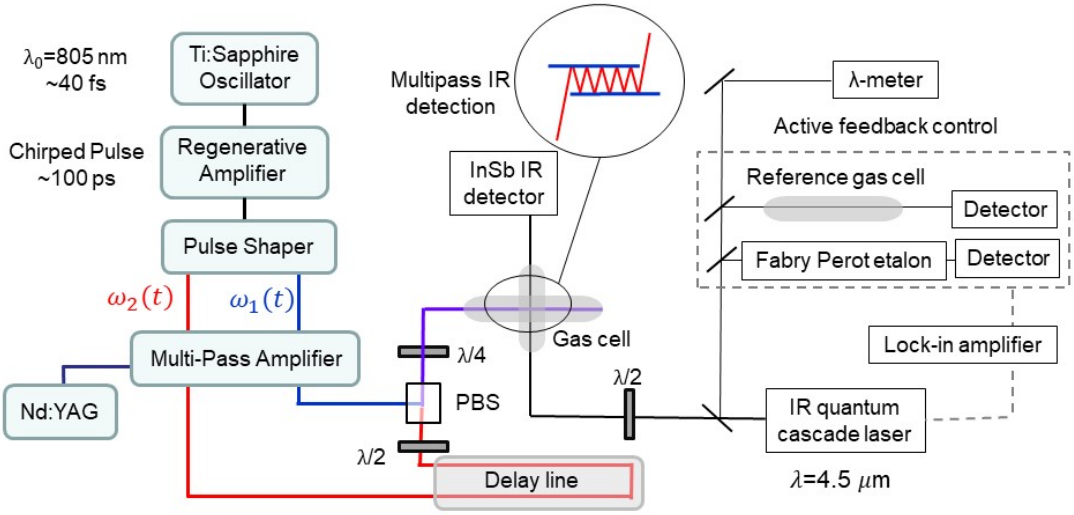

Figure 2. Schematic diagram of the optical-centrifuge transient-absorption spectrometer. The polarization of the pulses and the IR probe are controlled with $\lambda/2$ and $\lambda/4$ waveplates. The centrifuge pulses are recombined in a polarizing beam cube (PBC).

Inverted CO rotational distributions were prepared using an optical centrifuge with tunable spectral bandwidth. Optical centrifuge pulses are formed by combining oppositely-chirped ultrafast laser pulses ω_1 and ω_2, each with an initial wavelength of λ=805 nm. The pair of pulses has opposite circular polarization; when they are combined in time and space, the result is a linearly polarized optical field that undergoes angular acceleration over the duration of the pulse, based on the instantaneous frequency difference of the two chirped pulses. During the 100 ps pulse, the angular frequency of the optical field is $\Omega_{oc}(t) = \frac{1}{2}(\omega_1(t) - \omega_2(t))$. Molecules with anisotropic polarizability are trapped in the optical field through an induced dipole interaction and are angularly accelerated into high energy rotational states with oriented angular momentum vectors.

The intensity profiles of the two optical centrifuge traps are shown in Figure 3a. The S1 optical trap used the full spectral bandwidth of the pulsed laser. The S2 reduced-bandwidth trap was made using a reflective notch filter to remove light from the positively-chirped pulse with wavelengths shorter than 780 nm. When the optical trap intensity drops below the minimum

trapping intensity, molecules are released from the field, resulting in an inverted rotational distribution. The steeper fall-off of the S2 trap yields a steeper drop-off in the high-J populations, as shown in Figure 1.

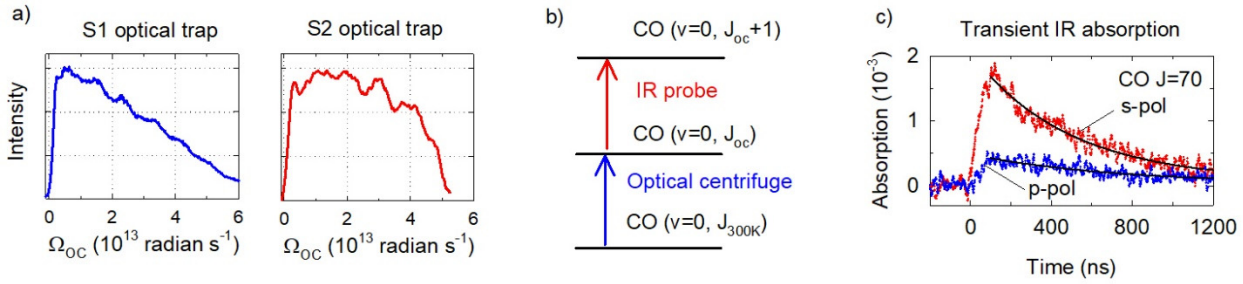

Figure 3. a) Profiles for the full-bandwidth (S1) and reduced-bandwidth (S2) optical centrifuge traps. b) Energy level scheme for optical excitation and transient IR probing of optically centrifuged CO. c) Transient absorption signals for CO J=70 with s-polarized and p-polarized IR light. The S1 trap was used for the signals shown here.

Individual rotational states of the optically centrifuged molecules were detected with high-resolution, polarization-resolved, transient IR absorption spectroscopy at λ=4.6 μm, using fundamental IR transitions for CO. Figure 3b shows the scheme for pulsed optical centrifugation of CO molecules, followed by IR absorption detection. The IR probe is the continuous-wave output of a quantum cascade laser that has a spectral resolution of $\Delta\nu_{IR}$<2×10^{-4} cm^{-1} (6 MHz). Transient absorption signals were measured following the centrifuge pulses.

The transient signals were collected as a function of the IR polarization to determine the extent to which the angular momentum of the optically centrifuged molecules is spatially oriented with respect to the optical propagation. Transient signals for CO J=70 are shown in Figure 3c for s- and p-polarized IR probing. The s-polarized IR probe polarization is perpendicular to the centrifuge propagation vector, while the p-polarization is parallel. Typically, transient signals were averaged for 100 laser pulses. The population decay for each signal was fit to an exponential decay curve, which is shown in black in Figure 3c and was used in the kinetic analysis. Molecules with a component of their angular momentum vector along the optical centrifuge propagation vector $\vec{k}_z$ yield signals for in-plane (IP) rotors while those with projections along the

x- and y-axes yield out-of-plane signals. The IP component at time t equals $2s(t) - p(t)$ and the OOP component equals $2p(t)$, where s and p are the s- and p-polarized signals, respectively.

The experiments used CO pressures of 2.5 Torr for the S1 optical trap and 5 Torr for the S2 trap at 298 K. The detector rise time was 50 ns and signals were analyzed starting at 100 ns following the optical centrifuge pulse. The average time between collisions is 42 ns for the 2.5 Torr data and 21 ns for the 5 Torr data, based on a Lennard-Jones collision rate constant of k_{LJ}=2.9×10^{-10} cm^3 molecule^{-1} s^{-1}.[31] The optical centrifuge pulse excites about 3% of the CO within the interaction region of the gas cell.

b. Modeling methods

State-to-state rate constants for rotational energy transfer in CO-CO collisions have not been determined experimentally for CO in extreme rotational states. In previous work, Hager, Heaven, and coworkers performed IR double-resonance experiments on CO rotational energy transfer and determined state-to-state energy transfer rate constants for the J=0-29 states.[21] They found that the statistical power exponential gap (SPEG) model was superior to the modified exponential gap and the energy corrected sudden with exponential-power gap models.[12,27] For up-collisions from state J to J' (with J<J'), the SPEG rate constant is given by Equation 1.

$$k_{JJ'} = a\left(\frac{\Delta E}{B}\right)^{-c} exp\left(-\frac{b\Delta E}{k_B T}\right) \qquad \text{for } J<J' \qquad (1)$$

Here, a, b, and c are fitting parameters, ΔE is the energy gap between rotational states, B is the rotational constant, and $k_B T$ is the average thermal energy.[12,27]

Hager, Heaven, and coworkers determined a, b, and c parameters using their CO state-to-state rate data for J=0-29 and the SPEG model.[21] We used their parameters to extrapolate state-to-state rate constants for CO J=30-90 at T=298 K. We first determined rate constants for up-collisions using Equation 1. State-to-state rate constants $k_{J'J}$ for down-collisions from J' to J were determined from up-collision rate constants and detailed balance, as in Equation 2.

$$k_{J'J} = k_{JJ'}\left[\left(\frac{g_{J\prime}}{g_J}\right) exp\left(-\frac{|\Delta E|}{k_b T}\right)\right] \qquad \text{for } J<J' \qquad (2)$$

Here, $g_{J'}$ and g_J are the degeneracies of the J' and J states, respectively. A state-specific total depletion rate constant k_{dJ} for CO state J was determined by summing rate constants for all up- and down-collisions for that state, as shown in Equation 3, for J'=0-90.

$$k_{dJ} = \sum_{J'} k_{JJ'} \qquad \text{for } J' \neq J \tag{3}$$

Figure 4a shows that the total depletion rate constants k_{dJ} generally decrease as a function of J. Figure 4b is a heat map of state-to-state rate constants for CO J=55-80. For a given initial J state, down-collisions have larger state-to-state rate constants than up-collisions, and up-collision rate constants decrease more strongly with J' than do down-collision rate constants for comparable $|\Delta J|$ values.

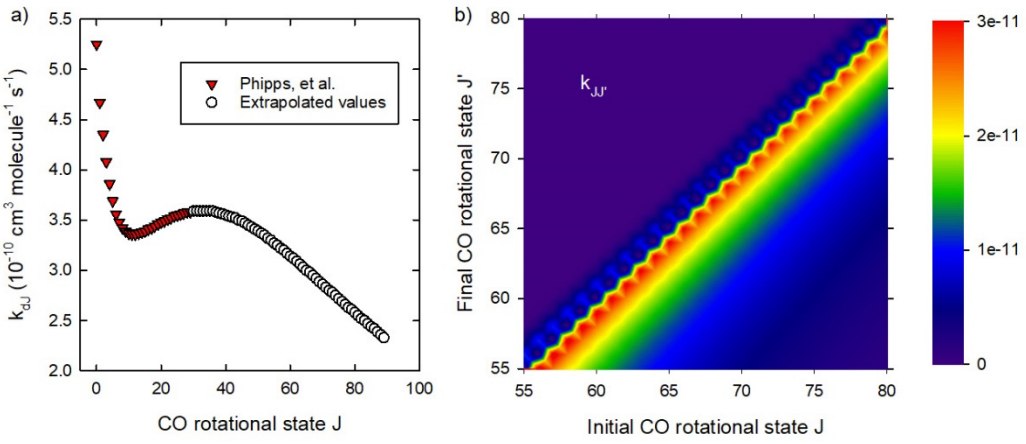

Figure 4. a) Overall depletion rate constants k_{dJ} for CO as a function of initial J state. b) Heat map of state-to-state rate constants for CO J=55-80. Rate constants have units of cm^3 molecule^{-1} s^{-1}.

Figure 5a shows state-to-state rate constants k'_{JJ} for a number of states as a function of the initial J state. Rates for elastic collisions with ΔJ=0 are not shown. For J=5, the magnitude of $k_{JJ'}$ is the essentially the same for ΔJ=+1 and ΔJ=-1 collisions. As J increases, the difference in rate constants for the down- and up-collisions increases. For J=75, the rate constant for ΔJ=-1 collisions is more than four times larger than that for ΔJ=+1 collisions. To illustrate the predominance of down-collisions relative to up-collisions in the relaxation of most J states, we separately summed the rate constants for down-collisions and for up-collisions to get an overall k_{down} and k_{up}, respectively. For states with J>7, we find that k_{down}>k_{up}, and the ratio of

$k_{down}$to k_{up} increases as with increasing J, as shown in Figure 5b. For J=80, k_{down} is nearly 30-times larger than k_{up}.

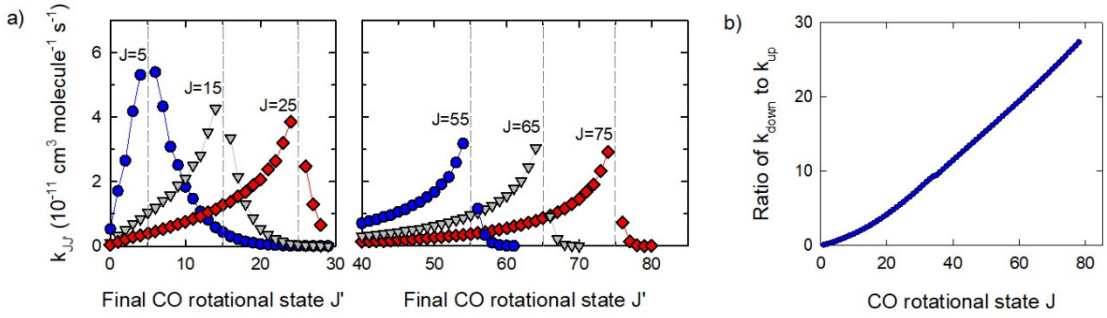

Figure 5. a) State-to-state rate constants for CO rotational energy transfer for selected initial states. Elastic collisions are excluded. b) Ratio of k_{down} to k_{up} as a function of initial J state.

The state-to-state rate constants for CO J=0-90 were used to simulate simultaneous rotational energy transfer events using a system of coupled differential rate equations. This set of master equations describes the population moving out of and into each rotational energy state up to J=80. Equation 4 shows the form of these equations.

$$\frac{dN_0}{dt} = \rho\left[-k_{d0}N_0 + \sum_{j\neq 0} k_{j0}N_j\right]$$

$$\frac{dN_1}{dt} = \rho\left[-k_{d1}N_1 + \sum_{j\neq 1} k_{j1}N_j\right] \qquad (4)$$

$$\vdots$$

$$\frac{dN_n}{dt} = \rho\left[-k_{dn}N_n + \sum_{j\neq n} k_{jn}N_j\right]$$

Here, N_n is the population in the n quantum state, ρ is the number density of bath gas, k_{dn} is the total depletion rate constant for state n, k_{jn} is the state-to-state rate constant from state j into state n (with $j \neq n$), and N_j is the population in state j.

The set of master equations is written in matrix notation, as in Equation 5.

$$\frac{d\boldsymbol{N}}{dt} = \rho \boldsymbol{K} \boldsymbol{N} \quad (5)$$

Here $\boldsymbol{K}$ is the rate constant matrix and $\boldsymbol{N}$ is an array for the number density in each rotational state. The off-diagonal elements of $\boldsymbol{K}$ are the state-to-state rate constants and the diagonal elements are the total depletion rate constants. The number density of individual states as a function of time has an analytical solution using matrices of this form, as described previously by Alexander, Hall, and Dagdigian.[33] Master equation simulations were run at 298 K using this approach, starting either with an idealized initial distribution, or with an initial distribution that was observed for optically centrifuged CO.

III. Results and discussion

Here we describe the results of master equation simulations and the kinetic analysis of optically centrifuge CO molecules. We start with a simulation for the relaxation of an ensemble of CO molecules initially in a single rotational state with J=66. We then present the time-dependent population data from the experiments, and compare the experimental results with the modeling results from the master equation analysis.

a. Model master equation simulations

We simulated the collisional relaxation of a sample of CO molecules initially in the J=66 rotational state, with a number density corresponding to 5 Torr at 298 K. Figure 6 shows the evolution of population initially in the J=66 state. At t=0 ns, the population in J=66 is unity, and at t= 5 ns (about ¼ of the gas kinetic collision time), 17% of the J=66 population has moved into other states, predominantly lower J states. The relaxation to lower states continues until an equilibrium thermal distribution is reached. The simulations show that the relaxation is complete by 10 gas-kinetic collisions. Note that at any time in the simulation, the population in states with J>66 is less than 2% of the initial population in J=66, showing that up-collisions play a minor role in the collisional relaxation.

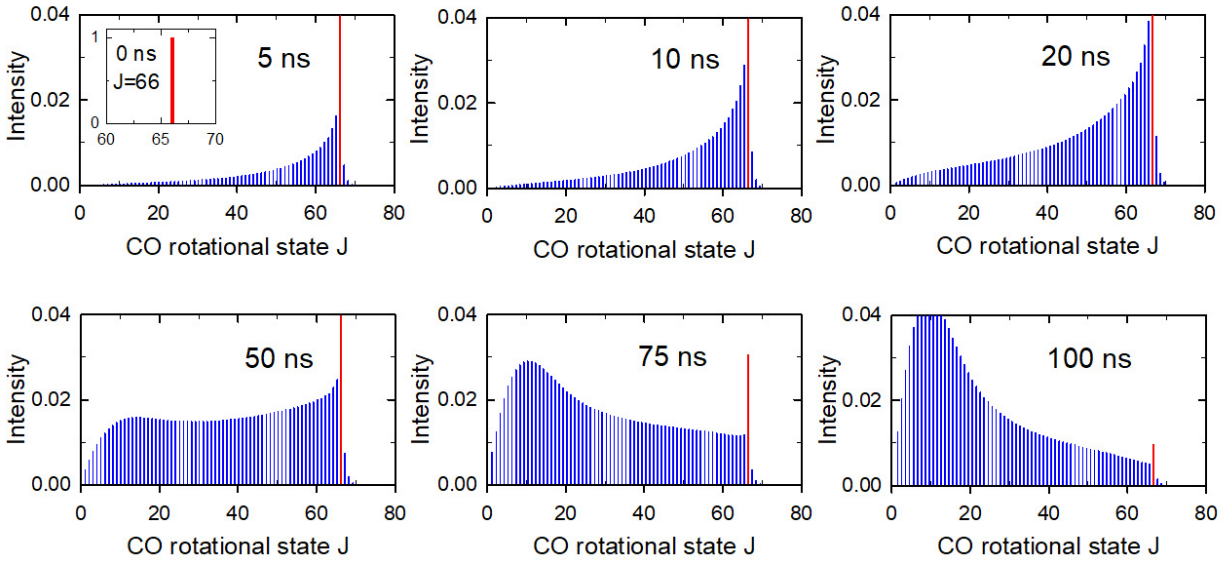

Figure 6. Simulation results showing the relaxation of CO J=66 in a 298 K bath of CO at 5 Torr. The simulation results at 100 ns correspond to 5 gas-kinetic collisions. The rotationally excited distribution reaches thermal equilibrium by 10 gas-kinetic collisions.

b. Kinetics of optically centrifuged CO from experiments

Here, we present an analysis of state-specific relaxation rates constants observed for optically centrifuged CO molecules. We focus on the time-dependent IP population data for the highest J states from the optical centrifuge experiments and determine overall rotational relaxation rate constants for the two optical traps.

Figure 7 shows the time evolution of CO populations in the highest-J states prepared with the S1 and S2 optical centrifuge traps, along with linear fits to the distributions at various times. The J-dependent populations at each time are well described by a linear fit, and with no constraints, the time-dependent linear fits intersect at J=82 for the S1 trap and at J=68 for the S2 trap, indicating that these are the highest states prepared in each trap and that collisional relaxation is moving population to lower, but not higher, rotational states.

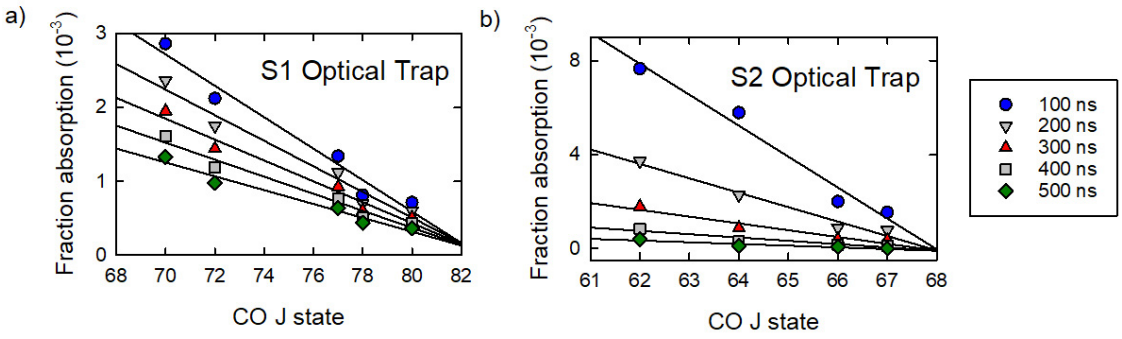

Figure 7. Time evolution of optically centrifuged CO rotational distributions based on high-resolution transient IR absorption measurements. The data in a) were observed for the S2 optical trap and those in b) are from the S1 optical trap.

We focus on the fall-off regions of the inverted distributions that include the J=70-80 states for the S1 trap and the J=62-67 states for the S2 trap. By studying the highest states observed in the experiments, we minimize the effect of population gains from relaxation of higher states. Two processes add population to a specific J state in the high-J region but the contributions from both are likely to be small in our experiments. First, the probability of population gain from up-collisions is low because these events have smaller state-to-state rate constants. Second, population gain from down-collisions is minimal because there is negligible population in higher J states, based on the intensity profiles of the optical centrifuge traps.

Observed depletion rate constants for optically centrifuged molecules were determined from net population change. CO molecules in state J relax through collisions with thermal bath molecules M with an observed rate constant k_{obs}, leading to a number of product states with quantum numbers J', where $J \neq J'$ as shown in Equation 6.

$$CO(J) + M \xrightarrow{k_{obs}} \sum_{J'}(CO(J') + M) \qquad \text{for } J' \neq J \tag{6}$$

In the limit of no population increases in state J, the observed rate constant k_{obs} equals k_{dJ}, the overall decay rate constant. For most states, the observed depletion rate is a lower limit to the actual depletion rate because of population gain from other states, and the difference in k_{obs} and k_{dJ} is minimized for the maximum J state in a distribution of centrifuged molecules. The number density of optically centrifuged molecules is a small fraction of the thermal sample, and

the observed relaxation has a pseudo-first order rate law, with rate constants $k'_{obs} = k_{obs}[M]$, where $[M]$ is the bath number density. The J-specific depletion rate is written as Equation 7.

$$\frac{d[CO(J)]}{dt} = -k_{obs}[CO(J)][M] = -k'_{obs}[CO(J)] \quad (7)$$

We first used a direct fit of the transient signals, as in Figure 3c, to determine decay constants as a function of J. Each transient signal was fit to a single exponential decay function to determine a decay constant τ, from which the rate constant $k_{obs}(\tau) = 1/(\tau[M])$ was obtained. The results are shown in Figure 8. Rate constants for the S1 optical trap are near $k_{obs}(\tau)$=2×10^{-11} cm^3 molecule^{-1} s^{-1}. Values for the S2 optical trap near $k_{obs}(\tau)$=(4 to 6)×10^{-11} cm^3 molecule^{-1} s^{-1}.

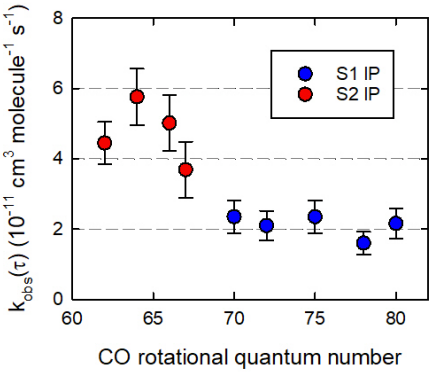

Figure 8. Rate constants $k_{obs}(\tau)$ for CO molecules prepared in the S1 and S2 optical traps were determined by fitting each transient signal to a single exponential decay.

Equivalently, the observed rate constants can be determined using the linear fits of the time-dependent distributions. Rate constants were determined from ratios of the integrated rate expression at different times t_1 and t_2, as in Equation 8.

$$k_{obs} = -ln\left(\frac{[CO(J)]_{t1}}{[CO(J)]_{t2}}\right)\left((t_1 - t_2)[M]\right)^{-1}. \quad (8)$$

An advantage of this approach is that the error in the rate constants is reduced because the time-dependent populations from the linear fits are used in the analysis. The S1 trap prepares CO states up to J=80 and the observed experimental relaxation rate constant based on Equation 8 is $k_{obs}(exp) = (2 \pm 0.1) \times 10^{-11}$ cm^3 molecule^{-1} s^{-1}. The same result is obtained using data at any two times shown in Figure 7, within two significant figures. We associate this decay rate constant with the highest J state formed in the optical trap, since the overall decay of this state has

minimal population gain from higher states. The S2 optical trap prepares CO with states only up to J=68, and its relaxation rate constant is more than twice that of the S1 trap, with $k_{obs}(exp) = (5 \pm 0.2) \times 10^{-11}$ cm^3 molecule^{-1} s^{-1}. These results are consistent with those obtained by fitting individual transient signals. The observed relaxation rate constants decrease with increasing quantum number J, just as do the extrapolated rate constants based on the SPEG model. However, the observed rate constants are lower than those predicted by the model and they have a stronger J-dependence.

c) Master equation modeling of CO relaxation kinetics

We ran master equation simulations to model the time evolution for the distributions of optically centrifuged molecules prepared in the S1 and S2 optical traps. Master equation modeling (MEM) started at t=0 with the CO distributions experimentally observed at t=100 ns (Figure 7), along with a 298 K thermal bath of CO molecules, at a pressure of 2.5 Torr for the S1 simulation and 5 Torr for the S2 simulation. Time-dependent populations N_n for individual rotation states were determined by simultaneously solving the set of coupled rate equations shown in Equation 4. The resulting time-dependent populations from the simulations are shown in Figure 9. The time increments between the simulated distributions in Figure 9 were chosen so that slope of the simulated data in each optical trap matched the slope of the observed distribution at t=200 ns (Figure 7).

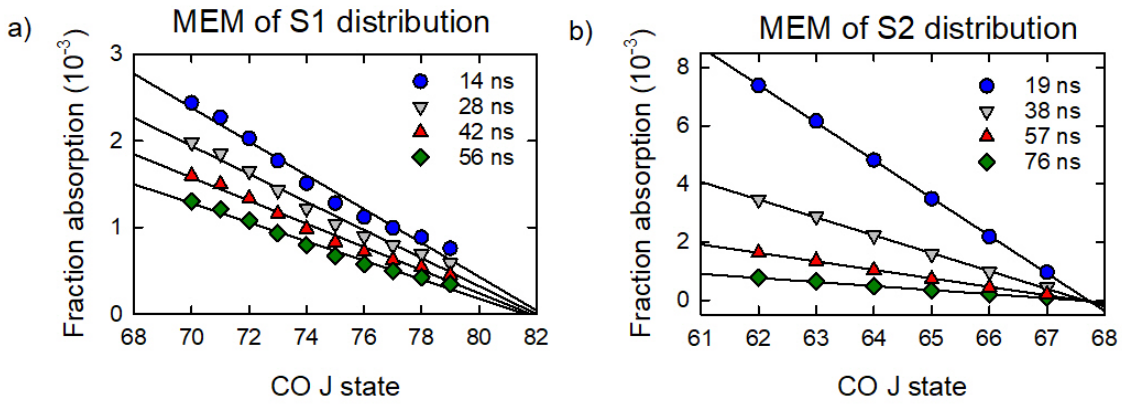

Figure 9. Master equation modeling (MEM) of the collisional rotational relaxation of CO molecules prepared in the a) S1 and b) S2 optical traps. The simulations used the observed distributions at t=100 ns as the initial t=0 distribution for the simulation. The simulation

times were selected based on similarity of the calculated distributions with the observed distributions.

Qualitatively, the relaxation behavior from the simulations is similar to what is observed in the experiments. The relaxation process is dominated by down-collisions, with population moving to lower states. The time-dependent simulation data are well fit by linear functions, and the points of intersection for the linear fits occur at similar J-states as for the experimental data. The fitting results intersect near J=83 for the S1 trap data and near J=68 for the S2 trap data. Quantitatively, however, the simulated relaxation occurs more rapidly than that observed in the experiments. The time steps in Figure 9 are 5-10 times smaller than the experimental time steps to reach comparable distribution slopes. Relaxation rate constants for the simulation data were determined using Equation 8, with values of $k_{obs}(MEM)$=2×10^{-10} cm^3 molecule^{-1} s^{-1} for the S1 trap data and $k_{obs}(MEM)$=2.5×10^{-10} cm^3 molecule^{-1} s^{-1} for the S2 data. The simulated decay rate constants are larger than the experimental values.

d) Comparison of experimental and simulated rate constants

It is informative to compare the decay rate constants $k_{df}(SPEG)$ from the SPEG model with the observed simulation rate constants $k_{obs}(MEM)$ and experimental rate constants $k_{obs}(exp)$. Figure 10 compares the rate constants for both optical traps. The simulation rate constants $k_{obs}(MEM)$ are lower than $k_{df}(SPEG)$ values. This difference mirrors the extent to which incoming population from higher states reduces the observed relaxation rate. The difference in rate constants depends on the initial distribution and is smallest for the highest J states of that distribution, showing that relaxation from higher J states is minimized for the highest states populated. From Figure 10, we see that for the S1 trap, $k_{obs}(MEM)$ for J=70 is only 70% of $k_{df}(SPEG)$, and for J=78, $k_{obs}(MEM)$ is 95% of $k_{df}(SPEG)$. For the S2 trap, $k_{obs}(MEM)$ for J=62 is 80% of $k_{df}(SPEG)$, and for J=67, $k_{obs}(MEM)$ is 95% of $k_{df}(SPEG)$. These values are consistent with intersecting fit results of J=82 for the S1 trap and J=68 for the S2 trap.

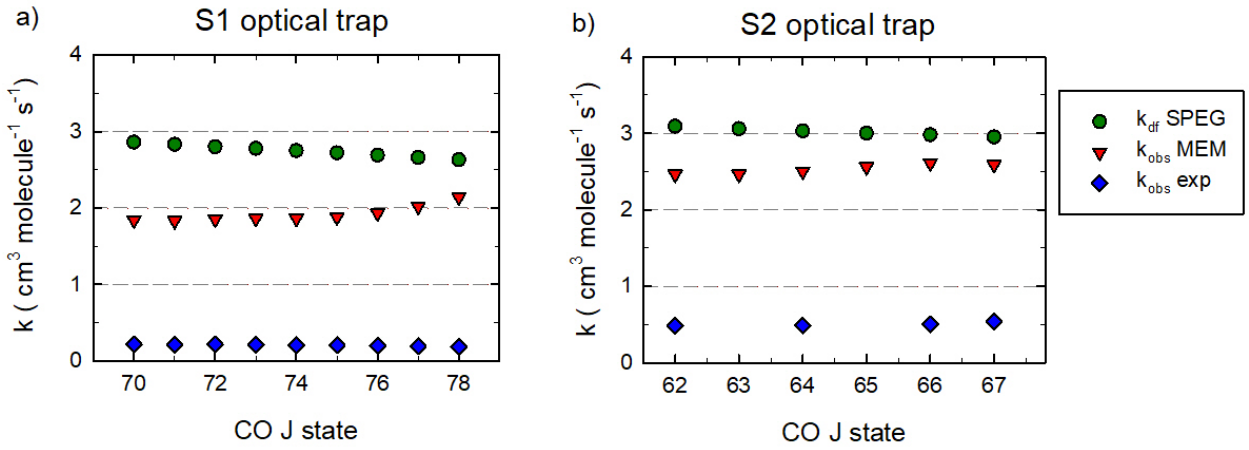

Figure 10. Comparison of J-specific rate constants for CO prepared with the a) S1 and b) S2 optical traps. Total depletion rate constants k_{dJ} from SPEG modeling are compared with k_{obs} values from master equation modeling (MEM) and experimental data.

Figure 10 shows that the experimentally observed rate constants $k_{obs}(exp)$ are smaller than the simulation rate constants $k_{obs}(MEM)$ by as much as an order of magnitude. Figure 11 shows the ratio of $k_{obs}(exp)$ to $k_{obs}(MEM)$. For the S1 trap, the ratio is near one-tenth, and for the S2 trap, the ratio is one-fifth. In addition, the observed decay rates from the measurements have a stronger J-dependence than is predicted by the SPEG model. In the experiments, the observed decay rate constant for CO J=68 (from the S2 trap) is 2.5 times larger than the rate constant for the J=82 state (from the S1 trap). In the SPEG model, k_{dJ} for J=68 is only 1.2 times larger than k_{dJ} for J=82.

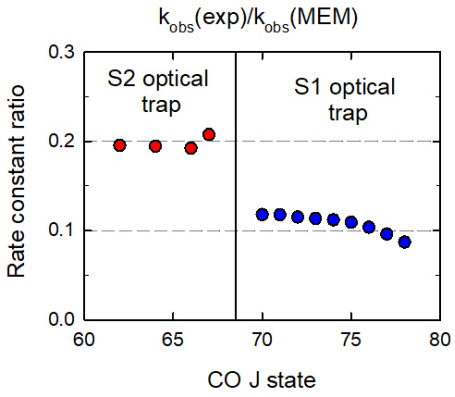

Figure 11. Ratio of experimental rate constants $k_{obs}(exp)$ to simulation rate constants $k_{obs}(MEM)$.

e) Dynamical aspects of collisional relaxation of optically centrifuged CO

Our results show that the SPEG model successfully mimics the time-evolution of the experimental distributions, as evidenced by the similarity of the experimental and simulated distributions shown in Figures 7 and 9. However, the SPEG model (with parameters from low-J data) overestimates the relaxation rate constants, by a factor of 10 for the S1 optical trap and a factor of 5 for the S2 optical trap. The observed decay constants also show a stronger J-dependence than is predicted by the SPEG model. These results indicate that additional factors contribute to the rotational relaxation process in the high energy regime, and these factors should be included in future models as data become available. Our studies report quantitative rate data for two rotational states of CO (J=68 and 82) and future studies using a tunable optical centrifuge should provide more extensive information on the J-dependence of collisional relaxation rates.

Our dynamical measurements of the relaxation process provide strong evidence that the angular momentum of optically centrifuged molecules inhibits their rotational energy transfer. The optical centrifuge prepares molecules with angular momentum vectors that are oriented, to a large degree, along the propagation vector of the optical beam. Most collisions of optically centrifuged molecules are expected to lead to changes in both rotational energy and lab-frame orientation. Figure 12 shows orientational anisotropy heats maps of the centrifuged molecules as a function of time for both optical traps. At the earliest measurement times, anisotropy values as high as $\boldsymbol{r}$=0.8 are seen for the highest J-states that are populated. Overall, the anisotropy values increase as a function of J. In addition, the anisotropy values of the higher-J states persist longer than those for lower-J states. Reduced reorientation rates of the higher-J molecules correlate with reduced relaxation rate constants.

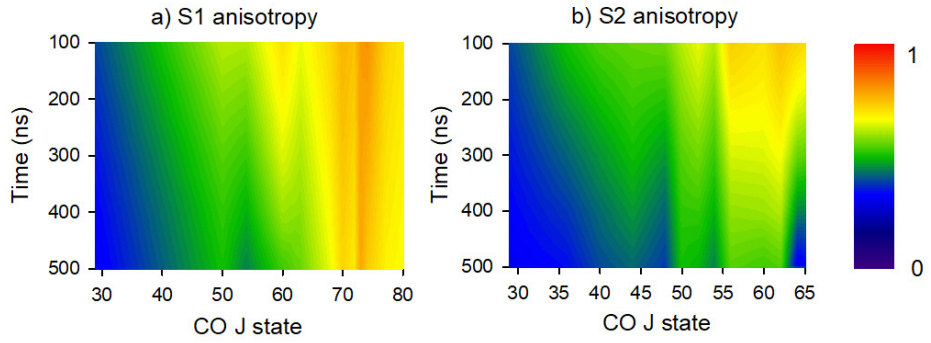

Figure 12. Orientational anisotropy values of CO prepared in the a) S1 and b) S2 optical centrifuge trap. initial anisotropy values increase as a function of J, while decay rate constants decrease with increasing J.

The orientational anisotropy decay rates were determined for the S1 trap data. Time-dependent anisotropies for individual states with J=63-68 are based on fitting J-dependent anisotropy values from polarization-resolved transient absorption measurements. The anisotropy values are shown in Figure 13a as a function of time, and were fit to exponential decay functions of the form $\boldsymbol{r}(t) = \alpha\, e^{-\beta t} + y_0$, with a baseline of y_0=0.33, corresponding to an isotropic distribution. The inset zooms in on the data and the fit results. The parameter β is a pseudo-first order decay constant related to the anisotropy decay constant k_r by $\beta = k_r[M]$, where $[M]$ is the number density of the bath gas. The resulting values of the anisotropy decay constant k_r are shown in Figure 13b, where the values decrease with increasing J. Notably, the rate constants k_r are smaller than $k_{obs}(exp)$ values by as much as a factor of ten. The number of collisions required to reach the $1/e$ anisotropy change is estimated by the ratio of the collision rate constant to the anisotropy decay rate constants. Figure 13c shows a strong J-dependence with the corresponding number of collisions ranging from 28 collisions for J=63 to 50 collisions for J=68.

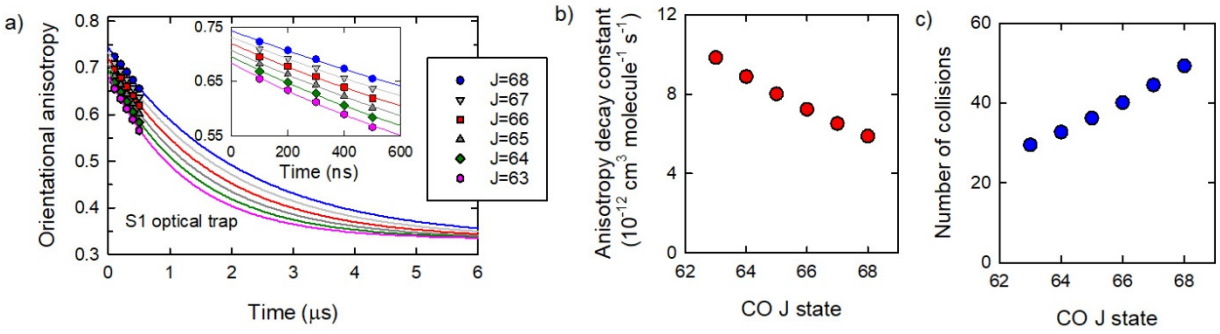

Figure 13. a) Orientation anisotropy decay curves for CO J=63-68, prepared in the S1 optical centrifuge trap. b) Orientational anisotropy decay constants for bimolecular collisions. C) Number of gas-kinetic collisions that corresponds to the observed anisotropy decay constant.

It is clear from these results that conserving both angular momentum and energy is difficult in the collisional relaxation of high energy rotors by thermal bath molecules. The energy gaps of CO with J=60 to 80 are 7-9 times larger than that for the most populated state (J=9) at 300 K. Collisions that induce angular momentum changes of ΔJ=-1 in optically centrifuged molecules require angular momentum increases in average thermal bath molecules of ΔJ=+7 to +9, a process that has low probability. Thus, the relaxation of optically centrifuged molecules by thermal bath molecules most likely involves those bath molecules that have energies well above the ensemble average, but with number densities that decrease exponentially with energy. In contrast, collisions of two optically centrifuged molecules most likely leads to resonant or near-resonant energy transfer with one molecule undergoing an angular momentum change of ΔJ=+1 and the other having ΔJ=-1, corresponding to no overall rotational relaxation.

The reduced probabilities of rotational relaxation and orientational anisotropy decay in optically centrifuged molecules have parallels to the classical physics of gyroscopes. In the presence of large amounts of angular momentum, molecules maintain their rotational energy and angular momentum orientation longer than if they had less angular momentum. The maximum reorientation angle of a gyroscope caused by impulsive collisions is inversely

proportional to the angular frequency of the gyroscope. Gyroscopes with larger amounts of angular momentum have larger angular frequencies and smaller reorientation angles. In the same way, at the molecular level, molecules in higher-J states have smaller rate constants for orientational anisotropy decay and rotational energy transfer.

Conclusions

One hundred years ago, Lindemann recognized the importance of activating and deactivating collisions on the kinetics of unimolecular reactions. Today, this mechanism continues to inform research of physical and chemical phenomena in many environments. In the work reported here, we investigate state-resolved rotational energy transfer in a high-energy regime that is made possible by the development of the optical centrifuge. Our studies highlight the importance of conserving both angular momentum and energy. The observed relaxation rates are significantly lower than those predicted by a statistical energy gap model that successfully describes the state-to-state kinetics of CO in a 300 K rotational sample. Future developments in modeling the rotational energy transfer of molecules with large amounts of angular momentum will be informed by studies using a tunable optical centrifuge, with which rotational state preparation can be controlled. Such studies will enable us to bridge the transition between the high-J and thermal energy regimes.

Author Contributions

Investigation: M. R Laskowski, T. J. Michael, H. M. Ogden and A. S, Mullin; Conceptualization: M. R, Laskowski, M. H. Alexander, and A. S. Mullin; Methodology: M. H. Alexander and A. S. Mullin; Formal analysis: M. R. Laskowski, T. J. Michael, and A. S. Mullin; Project administration and funding acquisition: A. S. Mullin; Writing: M. R. Laskowski and A. S. Mullin.

Conflicts of Interest

There are no conflicts to declare.

Acknowledgements

The authors acknowledge research support from the US National Science Foundation (CHE-18000531).

References

1. F. A. Lindemann, *Trans. Faraday Soc.*, 1922, **17**, 598.
2. C. N. Hinshelwood, *Proc. Roy. Soc. (A)*, 1927, **113,** 230.
3. O. K. Rice and H. C. Ramsperger*, J. Amer. Chem. Soc.*, 1928, **50**, 617.
4. L. S. Kassel, *J. Phys. Chem.*, 1928, **32**, 1065.
5. R. A. Marcus and O. K. Rice, *J. Phys. Colloid Chem.,* 1951, **55**, 1951.
6. R. A. Marcus, *J. Chem. Phys.,* 1952, **20**, 359.
7. H. M. Rosenstock, M. B. Wallendtein, A. L. Wahrhaftig and H. Eyring, *Proc. Nat. Acad. Sci. USA*, 1952, **38**, 667.
8. J. T. Yardley, *Introduction to Molecular Energy Transfer* (Academic Press, New York, 1980), Chap. 10.
9. A. J. Mccaffery, M. J. Proctor and B. J. Whitaker, *Ann. Rev. Phys. Chem.*, 1986, **37**, 223.
10. R. B. Kurzel, J. I Steinfeld, D. A. Hatzenhurler and G. E. Leroi, *J. Chem. Phys.*, 1971, **55**, 4822.
11. J. B. Cohen, E. B. Wilson, *J. Chem. Phys.,* 1973, **58**, 442.
12. D. E. Pritchard, N. Smith, R. D. Driver and T. A. Brunner, *J. Chem. Phys.*, 1979, **70**, 2115.
13. J. A. Barnes, M. Keil, R. E. Kutina and J. C. Polanyi, *J. Chem. Phys.,* 1980, **72**, 302.
14. S. L. Dexheimer, M. Durand, T. A. Brunner and D. E. Pritchard, *J. Chem. Phys.,* 1982, **76**, 4996.
15. J. D. Tobiason, A. L. Utz and F. F. Crim, *J. Chem. Phys.,* 1992, **97**, 7437.

16. G. P. Perram, D. A. Massman and S. J. Davis, *J. Chem. Phys.,* 1993, **99**, 6634.
17. C. A. Taatjes and S. R. Leone, *J. Chem. Phys., 1988,* **89**, 302.
18. Q. Liu, D. Yang and D. Xie, *J. Phys. Chem. A,* 2021, **125**, 349.
19. Y. Rudich, R. J. Gordon, E. E. Nikitin and R. Naaman, *J. Chem. Phys.,* 1992, **97**, 7437.
20. P. L. James, I. R. Sims, I. W. M. Smith, M. H. Alexander, M. A. Yang*, J. Chem. Phys., 1998,* **109**, 3882.
21. S. T. Phipps, T. C. Smith, G. D., Hager, M. C. Heaven, J. K. McIver and W. G. Rudolph, *J. Chem. Phys.,* 2002, **116**, 9281.
22. L. A. Mertens, H. Labiad, O. Denis-Alpizar, M. Fournier, D. Carty, S. D. Le Picard, T. Stocklin and I. R. Sims, Chem. Phys. Lett., 2017, 683, 521.
23. D. Forthomme, M. L. Hause, H.-G. Yu, P. J. Dagdigian, T. J. Sears and G. E Hall, *J. Phys. Chem. A,* 2015, **119**, 7439.
24. Millot, *J. Chem. Phys.,* 1990, **93**, 8001.
25. J. P. Looney, G. J. Rosasco, L. A. Rahn, W. S. Hurst and J. W. Hahn, *Chem. Phys. Lett.,* 1989, **161**, 232.
26. M. L. Koszykowski, L. A, Rahn, R. E. Palmer and M. E. Coltrin, *J. Phys. Chem.,* 1987, **91**, 41.
27. T. A. Brunner and D. Pritchard, *Adv. Chem. Phys.,* 1982, **50**, 589.
28. B. C. Sanctuary, *Chem. Phys. Lett.,* 1979, **62**, 378.
29. DePristo, H. Rabitz, *J. Chem. Phys.,* 1979, **71**, 850.
30. D. M. Villeneuve, S. A, Aseyev, P. Dietrich, M. Spanner, M. Y. Ivanov, P. B. Corkum, *Phys. Rev. Lett.,* 2000, **85**, 542.
31. T. J. Michael, H. M. Ogden and A. S. Mullin, *J. Chem. Phys.,* 2021, **154**, 134307.
32. M. J. Murray, H. M. Ogden and A. S. Mullin, *J. Chem. Phys.,* 2017, **147**, 154309.
33. M. H. Alexander, G. E. Hall and P. J. Dagdigian, *J. Chem. Ed.*, 2011, **88**, 1538.